



# Axial plane single-molecule super-resolution microscopy of whole cells

SHA AN,<sup>1,2,3,4,14</sup> KARL FERDINAND ZIEGLER,<sup>1,14</sup> PEIYI ZHANG,<sup>1</sup> YU WANG,<sup>5,6</sup> TIM KWOK,<sup>7</sup> FAN XU,<sup>1</sup> CHENG BI,<sup>1</sup> SANDRO MATOSEVIC,<sup>8</sup> PENG YIN,<sup>5,6</sup> TONGCANG LI,<sup>2,9,12</sup> AND FANG HUANG<sup>1,10,11,13</sup>

<sup>1</sup>Weldon School of Biomedical Engineering, Purdue University, West Lafayette, IN 47907, USA

<sup>2</sup>Department of Physics and Astronomy, Purdue University, West Lafayette, IN 47907, USA

<sup>3</sup>State Key Laboratory of Transient Optics and Photonics, Xi'an Institute of Optics and Precision Mechanics, Chinese Academy of Sciences, Xi'an 710119, China

<sup>4</sup>University of Chinese Academy of Sciences, Beijing 100049, China

<sup>5</sup>Wyss Institute for Biologically Inspired Engineering, Harvard University, Boston, MA 02115, USA

<sup>6</sup>Department of Systems Biology, Harvard Medical School, Boston, MA 02115, USA

<sup>7</sup>Birck Nanotechnology Center, Purdue University, West Lafayette, IN 47907, USA

<sup>8</sup>Department of Industrial and Physical Pharmacy, Purdue University, West Lafayette, IN 47907, USA

<sup>9</sup>School of Electrical and Computer Engineering, Purdue University, West Lafayette, IN 47907, USA

<sup>10</sup>Purdue Institute for Integrative Neuroscience, Purdue University, West Lafayette, IN 47907, USA

<sup>11</sup>Purdue Institute of Inflammation, Immunology and Infectious Disease, Purdue University, West Lafayette, IN 47907, USA

<sup>12</sup>tcli@purdue.edu

<sup>13</sup>fanghuang@purdue.edu

<sup>14</sup>S.A. and K.F.Z. contributed equally to this work

**Abstract:** Fluorescence nanoscopy has become an indispensable tool for studying organelle structures, protein dynamics, and interactions in biological sciences. Single-molecule localization microscopy can now routinely achieve 10–50 nm resolution through fluorescently labeled specimens in lateral optical sections. However, visualizing structures organized along the axial direction demands scanning and imaging each of the lateral imaging planes with fine intervals throughout the whole cell. This iterative process suffers from photobleaching of tagged probes, is susceptible to alignment artifacts and also limits the imaging speed. Here, we focused on the axial plane super-resolution imaging which integrated the single-objective light-sheet illumination and axial plane optical imaging with single-molecule localization technique to resolve nanoscale cellular architectures along the axial (or depth) dimension without scanning. We demonstrated that this method is compatible with DNA points accumulation for imaging in nanoscale topography (DNA-PAINT) and exchange-PAINT by virtue of its light-sheet illumination, allowing multiplexed super-resolution imaging throughout the depth of whole cells. We further demonstrated this proposed system by resolving the axial distributions of intracellular organelles such as microtubules, mitochondria, and nuclear pore complexes in both COS-7 cells and glioblastoma patient-derived tumor cells.

© 2019 Optical Society of America under the terms of the [OSA Open Access Publishing Agreement](#)

## 1. Introduction

Light microscopy allows the direct observation of biological specimens with molecular specificity. However, the diffraction limit restricts the resolution of conventional light microscopy to ~200 nm in lateral and ~500 nm in axial directions. This century-old barrier has restricted our understanding of protein functions, interactions, and dynamics in the cellular context, particularly at the sub-micron to nanometer length scale [1]. The invention of super-resolution microscopy methods, such as stimulated emission depletion microscopy (STED) [2–4], structured

illumination microscopy (SIM) [5–7], and single-molecule localization microscopy (SMLM) [8–10], overcomes this resolution barrier and improves the achievable resolution by a factor of ~10. Specifically, SMLM uses the switching capabilities of certain fluorescent probes (e.g. organic dyes or fluorescent proteins) to allow detection and localization of isolated single emitters at different time frames. Instead of pixel-based images, SMLM results in a list of single-molecule positions in two-dimension (2D), three-dimension (3D) and/or time dimension, from which the reconstruction reveals subcellular features and dynamics at 10–50 nm resolution [11–18].

While 2D SMLM allows capturing super-resolution images in the lateral direction, cellular structures organized along the axial direction (e.g. cytokinetic apparatus or nuclear envelope) mandate the lateral imaging plane to be scanned throughout the cell or tissue specimens, a time-consuming process. In addition, alignment procedures of the reconstructed super-resolution volumes are prone to misalignment and image artifacts especially in presence of specimen-induced aberrations [19]. Although the conventional light-sheet fluorescence microscopy (LSFM) [20–22] can directly obtain the axial plane information by using two orthogonal objectives, the system limits the use of objectives with high numerical apertures (NA) which is important for SMLM, and restricts the sample mounting strategy, making it difficult to study cells prepared on regular coverslips.

Single high-NA objective lens (e.g. NA = 1.4, as used in this study) is capable of generating high-quality light sheet in the axial plane. However, only the lateral plane can be captured in conventional SMLM experiments and therefore unable to take direct advantage of the self-generated light sheet [23,24]. By designing a specialized microfluidic sample mounting system with a mirror surface, sSPIM [25] and SO-LSM [26] converted the axial light sheet to the lateral direction allowing SMLM with single objective lens. In addition, by using a prism reflected and tilted light sheet generated by a separate objective lens, TILT3D [27] enabled light-sheet illumination in SMLM without the specialized microfluidic-mirror system. However, these developments coupled the light sheet position with one or more sample translation directions resulting in complicated optical readjustments when translating a specimen from one location to another. It is worth mentioning that, Li *et al.* provided a novel technique, termed axial plane optical microscopy (APOM) [28], which used a remote objective lens and a 45° tilted mirror to convert the axial information to the lateral plane and re-image onto a camera. In this case, the axial plane information could be directly imaged by single shot without scanning. This fast and high-contrast imaging approach is particularly suitable for studying thick samples and live cells.

In this work, we developed an axial plane SMLM integrating the single-objective light-sheet illumination and axial plane optical imaging with single-molecule super-resolution microscopy to resolve nanoscale cellular architecture along the axial (or depth) dimension. This system has a similar optical design as the recently published oblique-plane single-molecule localization microscopy (obSTORM) [29] but focusing on the axial plane super-resolution imaging utilizing two high-NA objective lenses (NA = 1.4). As one of the unique advantages of the axial plane SMLM system, the imaging plane overlaps with the illumination plane formed by a highly confined light sheet generated by the same objective lens for collecting fluorescence emission. This makes the system compatible with DNA points accumulation for imaging in nanoscale topography (DNA-PAINT) as well as its multiplexed version exchange-PAINT [30–35] allowing multiplexed super-resolution imaging throughout the depth of a specimen. In this case, utilizing the same type of fluorophore conjugated to orthogonal DNA strands for sequential axial plane multiplexed imaging requires a single laser source for excitation and is free of chromatic aberrations and distortions using a single emission channel. We demonstrated the applications of the presented system by resolving the axial distributions of cellular organelles and macromolecular assemblies such as microtubules, mitochondria, and nuclear pore complexes in both COS-7 cells and glioblastoma patient-derived tumor cells (GBM10).

## 2. Methods and materials

### 2.1. The optical setup of the axial plane SMLM

The complete optical diagram of the axial plane SMLM is shown in Fig. 1(A).

In the excitation part, three lasers of 642 nm (2RU-VFL-P-2000-642-B1R, MPB Communications Inc.), 488 nm (Cobolt 06-MLD 488 nm 200 mW, Cobolt Inc.) and 405 nm (DL405-100, CrystaLaser) wavelengths were combined by two dichroic mirrors (Di1, LM01-503-25; Di2, FF01-430/LP-25, Semrock), and then modulated by an acousto-optic tunable filter (AOTF, AOTFnC-400.650-TN, AA OPTO-ELECTRONIC). Thereafter, all the lasers were coupled into a single-mode polarization-maintaining fiber (P1-405BPM-FC, Thorlabs). An achromatic lens (L5,  $f = 20$  mm, AC080-020-A-ML, Thorlabs) was used for collimating the output laser beam. A light sheet was generated by a pair of cylindrical lenses (CL1,  $f = 200$  nm and CL2,  $f = 20$  nm), and its thickness was further confined by placing a slit in the focal plane of CL2. After passing through L6 ( $f = 175$  nm) and an oil-immersion objective lens (Obj1, UPLSAPO 100XO, NA = 1.4, OLYMPUS), hereafter referred to as imaging objective, a quad-band dichroic mirror (Di3, Di03-R405/488/561/635-t3-25X36, Semrock) was placed between these two components to separate the excitation and emission light, a vertical light sheet with  $\sim 1.19 \mu\text{m}$  thickness was created on the sample position for illuminating a certain axial slice. Epi-illumination mode can be switched from light-sheet illumination mode by removing the light-sheet creation part marked with the blue dashed rectangle. Samples were mounted on a custom-made stage with four degrees of freedom in  $x$ ,  $y$ ,  $z$  and rotation about  $z$ . The translations were carried out by stepper motors and piezo stages (MAX341/M, Thorlabs), while a rotation stage (U-651, PI) was assembled on top of the translation stages for controlling the rotation of the sample to allow imaging a particular vertical section of a specimen using a stationary light sheet beam.

In the emission part, the fluorescence signal was collected by the imaging objective Obj1, transmitted through Di3, and relayed to a polarizing beam splitter (PBS252, Thorlabs) by a 4f system with two achromatic lenses L7 and L8 ( $f = 175$  nm). The polarizing beam splitter divided the emission light into two parts. The reflected part was used to image the lateral plane information on a complementary metal-oxide-semiconductor (CMOS) camera (UI-3060CPM-GL, IDS Imaging Development Systems GmbH). The transmitted part passed through a quarter-wave plate (QWP, AHWP05M-600, Thorlabs) and formed an intermediate image at the focal point of another objective lens (Obj2, identical with Obj1), hereafter referred to as remote objective. Then, a  $45^\circ$  tilted mirror was used to convert the axial plane image into the lateral plane with its surface coinciding on the focal point of Obj2. Since the working distance of the high-NA objective was as small as 0.13 mm, only the edge of the  $45^\circ$  tilted mirror was used. Therefore, the mirror needs a high-quality reflecting surface as well as a straight edge. Here, the mirror was made using a cleaved silicon wafer coated by a thin layer of aluminum (150 nm), resulting in a straight and sharp edge. This wafer was glued on a right-angle prism for setting the  $45^\circ$  angle. Then, we fixed the  $45^\circ$  tilted mirror on a six-axis kinematic mount (K6XS, Thorlabs), which was placed on a translation stage (M-460A, Newport) controlled by a picomotor actuator (8303, Newport). With this configuration, the backward emission light, reflected by the  $45^\circ$  tilted mirror, was collected by the remote objective, and passed through the QWP again. The polarizing beam splitter and the QWP were combined to allow the p-polarized fluorescence signal to be detected by a scientific complementary metal-oxide-semiconductor (sCMOS) camera with high sensitivity and low noise (Orca-Flash4.0LT, Hamamatsu). Two achromatic lenses L11 ( $f = 200$  mm) and L12 ( $f = 100$  mm) were used for adjusting the magnification to map an effective pixel size of 130 nm in the specimen [36]. An excitation cleanup filter (CF, FF01-390/482/563/640-25, Semrock) and a matched emission filter (EF, FF01-446/523/600/677-25, Semrock) were used in this system. In addition, a white LED was placed on top of the Obj1 for imaging in the transmission mode.

## 2.2. Sample preparation

**Single layer beads sample preparation:** A cleaned 25-mm-diameter round coverslip was incubated with 200  $\mu$ L Poly-L-Lysine (P4707, Sigma-Aldrich) for 30 min. Then the coverslip was rinsed thrice with deionized water, dried and incubated with 200  $\mu$ L 100 nm-diameter crimson beads (custom-designed, Invitrogen) diluted to 1:10<sup>5</sup> in Phosphate Buffered Saline (PBS) (10010023, Gibco) for 30 min. After rinsing thrice with deionized water, the coverslip was mounted on a custom-made sample holder, and 20  $\mu$ L 97% TDE (166782, Sigma-Aldrich) was added on top of the coverslip. Another pre-cleaned coverslip was carefully placed on top of it to extend the buffer over the whole coverslip. The excessive buffer was removed with tissue papers. Finally, the sample was sealed with the two-component silicon dental glue (picodent twinsil speed 22, Dental-Produktions und Vertriebs GmbH, Wipperfürth).

**Agarose embedded beads sample preparation:** 8 mg of agarose (A9045-5G, Sigma-Aldrich) was added to 400  $\mu$ L beads diluted to 1:10<sup>5</sup> in PBS. The mixture was heated to 69 °C for 5–10 min and vortexed to blend evenly. A cleaned coverslip was mounted on a custom-made sample holder. Then, 400  $\mu$ L prepared mixture was added on top of the coverslip. Another pre-cleaned coverslip was immediately placed on top of it to extend the mixture over the whole coverslip. Then the sample was put in refrigerator to solidify. Finally, the sample was sealed with the two-component silicon dental glue.

**Immunofluorescence labeling:** Mammalian cells (COS-7 or GBM10) were cultured at 37 °C with 5% CO<sub>2</sub> on autoclaved coverslips. The culture media contained 10% FBS (30-2020, ATCC), 1% PS (15140122, Gibco) in DMEM (30-2002, ATCC). Cells were fixed and immune-labeled when the confluence reached ~80%. **Mitochondria or microtubules labeling:** COS-7 cells were fixed for 15 min at room temperature (RT) with 37 °C pre-warmed 3% Paraformaldehyde (PFA, 15710, Electron Microscopy Sciences) and 0.5% Glutaraldehyde (GA, 16019, Electron Microscopy Sciences) in PBS, then rinsed twice with PBS and treated for 7 min with freshly prepared fluorescence quenching buffer containing 0.1% NaBH<sub>4</sub> (452882, Sigma-Aldrich) in PBS. After rinsing thrice with PBS, cells were permeabilized and blocked for 30 min with 3% BSA (001-000-162, Jackson ImmunoResearch) and 0.2% Triton X-100 (X100, Sigma-Aldrich) in PBS, gently rocked at RT. After blocking, cells were incubated with the primary antibody diluted to 1:500 in 1% BSA and 0.2% Triton X-100 in PBS, overnight at 4 °C. The primary antibodies for mitochondria and microtubules were anti-Tom20 (Rabbit polyclonal, sc-11415, Santa Cruz Biotechnology) and anti- $\alpha$ -tubulin (T5168, Sigma-Aldrich), respectively. Cells were subsequently rinsed thrice for 5 min each time with wash buffer (0.05% Triton X-100 in PBS), and then incubated with the secondary antibody diluted to 1:500 in 1% BSA and 0.2% Triton X-100 in PBS for 4 h. The secondary antibodies for mitochondria and microtubules were AF647-anti-rabbit (A21245, Molecular Probes) and AF647-anti-mouse (A21236, Molecular Probes), respectively. Then cells were rinsed thrice for 5 min each time with wash buffer and post-fixed with 4% PFA in PBS for 10 min at RT. After rinsing thrice with PBS, cells were stored in PBS at 4 °C. **DNA-PAINT labeling:** Only the secondary antibody was replaced to DNA-conjugated anti-mouse P1 and/or anti-rabbit P4 according to the primary antibody, and the other labeling operations followed the above-mentioned protocol. **Nuclear pore complex labeling:** Cells were rinsed for 20 s with 37 °C pre-warmed 2.4% PFA in PBS, then extracted with 37 °C pre-warmed 0.4% Triton X-100 in PBS for 3 min. After extraction, cells were fixed with 37 °C pre-warmed 2.4% PFA in PBS for 30 min at RT, then rinsed thrice with PBS and treated for 7 min with freshly prepared fluorescence quenching buffer (0.1% NaBH<sub>4</sub> in PBS). After rinsing thrice with PBS, cells were permeabilized and blocked for 1 h with 5% BSA in PBS, gently rocked at RT. Then, after blocking, cells were sequentially incubated with the primary antibody Nup98 (2598S, Cell Signaling Technology) and secondary antibody AF647-anti-Rabbit (A21245, Molecular Probes), the labeling operations followed the above-mentioned protocol.

**Super-resolution imaging buffer and mounting:** The coverslip with cells was mounted in the custom-made sample holder. The imaging buffer was added to the center of the coverslip. For imaging Alexa Fluor 647 probes, the imaging buffer comprised 2.5 mM PCA (37580, Sigma-Aldrich), 50 nM PCD (P8279, Sigma-Aldrich), 10 mM MEA (M6500, Sigma-Aldrich), 50 mM BME (M3148, Sigma-Aldrich), and 2 mM COT (138924, Sigma-Aldrich) in dSTORM base buffer (pH = 8.0). The dSTORM base buffer contained 10% (w/v) glucose, 50 mM Tris (JT4109, Avantor) and 50 mM NaCl (S271-500, Fisher Scientific). ~20 drops of mineral oil were added on top of the imaging buffer to seal the sample. For multiplexed imaging with the exchange-PAINT technique, the imaging buffer contained 2 nM “imager” strands (DNA-conjugated Atto 655 P4 for Tom20 and P1 for  $\alpha$ -tubulin) and 500 mM NaCl in PBS.

### 2.3. Data acquisition

**Point spread function (PSF) acquisition using fluorescence beads:** A prepared single layer fluorescence beads sample was placed on the sample stage controlled by piezo stages. After aligning the 45° tilted mirror, the axial plane image of a bead was identified on the camera. Then the PSF data was taken by scanning the sample along the y-axis with 100 nm step size. The power density of the illumination light sheet was ~0.3–0.6 kW/cm<sup>2</sup>.

**Single-color SMLM imaging data acquisition:** An agarose embedded fluorescence beads sample was used for aligning the 45° tilted mirror. The beads sample was excited by the 642 nm laser with an intensity of 0.3–0.6 kW/cm<sup>2</sup>. We optimized the imaging system by adjusting the tilted mirror such that the illumination light sheet plane overlapped with the imaged axial plane on the camera. After optimization, the beads sample was replaced with the cell specimen. Before SMLM data acquisition, the specimen was excited at a high laser power to push most fluorophores into the dark state therefore reduce the background. The SMLM imaging was performed at 20–50 frames/s. The total number of frames per dataset ranged from 10,000 to 30,000 frames. The power density of the light-sheet illumination was ~2–5 kW/cm<sup>2</sup>.

**Two-channel SMLM imaging data acquisition:** After aligning the 45° tilted mirror following the above protocol, cell specimen was placed on the sample stage. A wide-field reference image under transmission light was recorded for two-channel alignment later. Then, the blinking dataset of the first channel was recorded at 20 frames/s for 20,000–30,000 frames. After data acquisition of the first channel was finished, the first imaging buffer was removed, the sample was washed thrice with PBS, and then the second imaging buffer was infused. The buffer exchange was accomplished by using a custom-made fluid exchange tool. This tool included two 1-meter-long thin plastic tubes connected with needles on all ends. The needle on one end of the tubing was inserted into the imaging medium, while the other needle was inserted into a syringe. One of the syringes/tubing combinations was used to draw buffer from the sample chamber and the other was used to infuse new buffer/imager strands to the system. Then, the blinking dataset of the second channel was recorded at 20 frames/s for 20,000–30,000 frames.

### 2.4. Single-molecule localization analysis

Here, the axial plane PSF was fitted with a 2D elliptical Gaussian function,

$$u_k(x, z) = I_0 \exp \left( -2 \frac{(x - x_0)^2}{w_x^2} - 2 \frac{(z - z_0)^2}{w_z^2} \right) + b, \quad (1)$$

where  $u_k(x, z)$  is the expected photon count for a given pixel  $k$ ,  $I_0$  is the peak intensity,  $(x_0, z_0)$  is the location of the fluorophore in the axial plane,  $w_x$  and  $w_z$  are the widths of the PSF in the  $x$  and  $z$  directions respectively, and  $b$  is the fluorescence background.

Maximum likelihood estimator (MLE) was used to fit data with Poisson statistics through maximizing the likelihood function,

$$L(\theta|D) = \prod_k \frac{u_k(x, z)^{d_k} e^{-u_k(x, z)}}{d_k!}, \quad (2)$$

where the likelihood of the parameter  $\theta$  given the data  $D$  is modeled as Poisson distribution given by the model  $u_k$  and the observed counts  $d_k$  at pixel  $k$ .

Drift correction was performed using a 2D redundant cross-correlation method [37,38]. The entire localization dataset was split into  $n$  segments (each segment contains 2,000 frames). For each segment, a 2D histogram was generated where the value in each pixel represents the number of localizations falling within that pixel. Cross-correlation was calculated to find the shift distance between each pair of segments, where the correlation peak with sub-pixel resolution was identified after Fourier interpolation [37]. In this process, for each pair of segments ( $i$  and  $j$ ), the shift distance can be obtained as  $(x_{shift}^{(i,j)}, z_{shift}^{(i,j)})$ . For all  $n$  segments, there are  $\frac{1}{2}n(n + 1)$  shift measurements,  $\{(x_{shift}^{(1,2)}, z_{shift}^{(1,2)}), \dots, (x_{shift}^{(i,j)}, z_{shift}^{(i,j)}), \dots, (x_{shift}^{(n-1,n)}, z_{shift}^{(n-1,n)})\}$ , forming an overdetermined system for  $(n - 1)$  independent shifts between adjacent segments  $(r_1, r_2, \dots, r_{n-1})$ . A temporary solution was found to minimize the overall error of the system using least square. This temporary solution was substituted back into all equations and residual errors were calculated. An equation from the system was removed if its error was larger than an empirical threshold (60 nm). This process was repeated until no equation gave an error larger than the threshold or the system of linear equations was no longer at full rank. In the case of two-channel imaging using exchange-PAINT, single molecule data were acquired first for Tom20 and then for  $\alpha$ -tubulin. For the first channel, we corrected the sample drift by 2D redundant cross-correlation method with the reference being the last data segment. For the second channel, the first segment was used as the reference to correct the drift. The sample was tightly fixed on the custom-made sample stage and we assumed that the stage shift during the brief buffer changing period was negligible. Future applications requiring long term stability of the system will benefit from active stage stabilization techniques, for example using transmission images [39] or large polystyrene beads for high precision feedback [40].

## 2.5. Three-dimensional axial plane point spread function

Assume that an intermediate image of an object is formed between the remote objective and the tilted mirror. Let this intermediate image lie on the  $x'y'z'$ -Cartesian coordinate system, with the positive  $z'$ -direction in the direction of the optical axis, pointing away from the exit pupil. After the  $\alpha/2$  degree tilted mirror, the intermediate image is rotated  $\alpha$  degree about the  $x'$ -axis in the counterclockwise direction. This rotated intermediate image will act as a new object for the rest of this imaging system and form the final image. Let the rotated intermediate image lie on the  $xyz$ -Cartesian coordinate system. The relationship between  $(x', y', z')$  and  $(x, y, z)$  can be described as,

$$\begin{bmatrix} x' \\ y' \\ z' \end{bmatrix} = \begin{bmatrix} 1 & 0 & 0 \\ 0 & \cos \alpha & -\sin \alpha \\ 0 & \sin \alpha & \cos \alpha \end{bmatrix} \begin{bmatrix} 1 & 0 & 0 \\ 0 & 1 & 0 \\ 0 & 0 & -1 \end{bmatrix} \begin{bmatrix} x \\ y \\ z \end{bmatrix} = \begin{bmatrix} x \\ y \cos \alpha + z \sin \alpha \\ y \sin \alpha - z \cos \alpha \end{bmatrix}. \quad (3)$$

In the axial plane SMLM system,  $\alpha = 90^\circ$ , where  $(x', y', z') = (x, z, y)$ . Therefore, the  $x$ - $z$  plane of the rotated intermediate image will be detected on the final image plane.

The detected image from a point source of unpolarized light, i.e. the 3D intensity point spread function  $I(x, y, z)$ , can be derived as:

$$I(x, y, z) = \frac{1}{2}(\lvert \vec{I}_A(x, y, z) \rvert^2 + \lvert \vec{I}_B(x, y, z) \rvert^2), \quad (4)$$

where  $\vec{I}_A$  and  $\vec{I}_B$  are two vectors initially defined in Kim *et al.* [41, Eq. (9)] with the spherical coordinate system.

Here, we modified the 2D intensity PSF into 3D together with the Spherical-to-Cartesian Coordinate transformation  $(k_x, k_y, k_z) \equiv (\frac{n}{\lambda} \sin\theta \cos\phi, \frac{n}{\lambda} \sin\theta \sin\phi, -\frac{n}{\lambda} \cos\theta)$ , then Eq. (4) can be derived as:

$$\vec{I}_j(x, y, z) = \left(\frac{\lambda}{n}\right)^2 \iint \vec{E}_j P(k_x, k_y) e^{-i2\pi[xk_x + (y \cos\alpha + z \sin\alpha)k_y + (y \sin\alpha - z \cos\alpha)k_z]} dk_x dk_y, \quad (5)$$

where  $j = A$  or  $B$ ,  $k_x k_y k_z$ -axes are parallel with  $x' y' z'$ -axes respectively,  $P(k_x, k_y)$  is the pupil function in  $k$  space with a length  $\rho = n/\lambda$ ,  $n$  is the refractive index of the immersion medium, and  $\lambda$  is the emission wavelength in vacuum [42,43]. The detailed description of the pupil function  $P(k_x, k_y)$  and electric field  $\vec{E}_j, j=A$  or  $B$  are defined in Kim *et al.* [41, Eqs. (5–6)].

### 3. Results

#### 3.1. Working principle and point spread function of the axial plane SMLM

Our design began with the axial plane optical microscopy (APOM) method [28]. A vertical slice of fluorescently stained biological specimen was excited by a light sheet generated using a high-NA objective lens ( $NA = 1.4$ ). The emitted fluorescence signal was collected by the same objective lens Obj1, making the system compatible with regular coverslip-mounted samples (Fig. 1(B)). A remote high-NA objective lens ( $NA = 1.4$ ) was used for both forming an intermediate image with its focal point coinciding on a mirror surface oriented  $45^\circ$  with respect to its optical axis, and collecting the backward reflected fluorescence signal from the  $45^\circ$  tilted mirror. This design effectively rotated the axial plane image to the lateral focal plane of the remote objective (Fig. 1(C) and (D)). To double the efficiency of the photon collection from single-molecule emissions, compared with previous APOM design [28], we combined a polarizing beam splitter with a QWP such that the p-polarized single-molecule fluorescence signal was transmitted, double passed through the QWP before being detected by an sCMOS camera. This design also allowed imaging both lateral and axial planes simultaneously (Fig. 1(A)). Comparing to conventional lateral plane SMLM, the presented axial plane SMLM decreased the light efficiency,  $\sim 7\%$  fluorescence emission was detected on account of 50% loss at the polarizing beam splitter, 36% at the remote objective and 78.36% because of the asymmetric pupil (Fig. 1(E)). Despite the significant loss of emitted photons, a reasonable signal-to-noise ratio (SNR) of single molecule emissions was achieved because of the compatibility of light-sheet illumination. This allowed us to reconstruct an axial plane super-resolution image without scanning through localizing the detected stochastically switching but isolated single-molecule emission patterns in the  $x$ - $z$  plane.

To characterize the PSF in the axial plane SMLM system, we extended a previous 2D analysis of APOM response [41] to 3D and compared the theoretical response function with the experimentally obtained PSF using fluorescence beads by scanning the sample stage in the  $y$  direction, perpendicular to the imaged  $x$ - $z$  plane. In comparison with an ideal PSF, we observed that our experimental PSF showed high similarity with the theoretical one, however, with a small amount of spherical aberration ( $127 \text{ m}\lambda$ , Fig. 1(F), and Appendix, Fig. 5(A)). Due to the asymmetric loss of fluorescence within the collection cone of the remote objective, induced by the  $45^\circ$  angle of the tilted mirror, the detected axial PSF evolved asymmetrically along the  $y$ -axis (Appendix, Fig. 5(A)). When the designed focus of the remote objective coincided

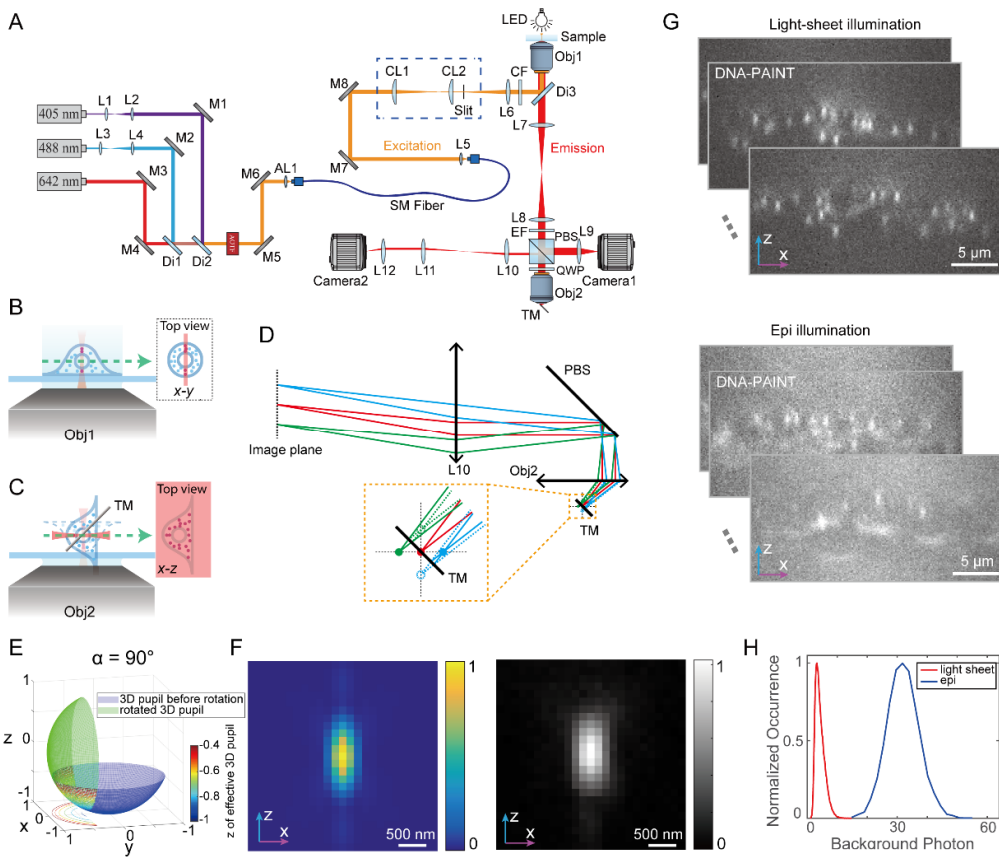


**Fig. 1.** Working principle schematics of the axial plane SMLM and experimental quantifications. (A) Optical diagram of the axial plane SMLM. The illumination method can be switched between light sheet and epi by adding or removing the light-sheet generating part marked with the blue dashed rectangle (a pair of cylindrical lenses and a slit). (B) Excitation and detection profile at the imaging objective. A vertical light sheet is used for exciting a thin slice of the specimen and the emission fluorescence is collected by the same objective lens. (C) Axial plane image formation diagram using a 45° tilted mirror above the remote objective. The 45° tilted mirror rotates the axial plane image of the specimen to the lateral focal plane of the remote objective. (D) Ray paths schematic showing the axial plane imaging concept (the dashed lines represent the effective incident rays to the tilted mirror, and the solid lines represent the effective reflected rays from the tilted mirror). (E) Effective 3D pupil of the axial plane imaging system. The mirror is placed  $\alpha/2$  degree ( $45^\circ$ ) to the  $x-y$  plane, the effective 3D pupil is shown as the overlapped area (jet) of the original pupil (blue) and the rotated pupil (green). (F) Comparison of a simulated ideal axial plane PSF (left) and an experimental PSF (right) of the SMLM system. (G) Example images from blinking dataset excited by the light-sheet illumination and epi illumination during single-molecule imaging with DNA-PAINT probes. (H) Normalized distribution of background photon estimation of the light-sheet illumination and epi illumination corresponding to G. The light-sheet illumination reduced the background ~11 fold compared to the epi illumination. L: lens; M: mirror; Di: dichroic mirror; AOTF: acousto-optic tunable filter; AL: aspheric lens; SM Fiber: single-mode optical fiber; CL: cylindrical lens; CF: cleanup filter; Obj1: imaging objective lens; Obj2: remote objective lens; EF: emission filter; PBS: polarizing beam splitter cube; QWP: quarter-wave plate; TM: tilted mirror. Scale bar: 500 nm in F, 5 μm in G.

on the mirror surface, we observed the elliptical shaped emission pattern with its long axis aligned with the  $z$  (axial) direction and the short axis aligned with the  $x$  direction (directions referencing to the sample plane). This elliptical PSF shape maintained within a  $y$ -range of 800 nm around the focal plane. The emission pattern started to differ significantly from the elliptical shape at  $\pm 500$  nm away from the focus. Considering that our axial plane SMLM system utilized light-sheet illumination with full width half maximum (FWHM) of  $1.19 \pm 0.04$   $\mu\text{m}$  (Appendix, Fig. 5(E)–(H)), we reasoned that the detected PSF from this narrowly illuminated sheet could be modeled as elliptical Gaussian with its long and short axes along the  $z$  and  $x$  directions respectively (Appendix, Fig. 5(I)). In addition, our axial plane SMLM system used two oil-immersion objectives with large NAs (1.4) for imaging specimens in aqueous environment which would result in the refractive index mismatch aberrations [44]. Under our present imaging conditions, we observed the elliptical PSF shape could be maintained in  $z$  direction over 20  $\mu\text{m}$  which was currently sufficient for single-molecule super-resolution experiments demonstrated here and for future live cell imaging tasks.

### 3.2. Super-resolution imaging of whole cells with the axial plane SMLM

To demonstrate the super-resolution capability of the light-sheet illuminated axial plane SMLM system, we imaged immuno-labeled  $\alpha$ -tubulin with Alexa Fluor 647 in fixed COS-7 cells. In comparison to the diffraction-limited axial plane image, the super-resolution image displayed distinct and isolated individual tubular structures and the overall interlaced microtubule network surrounding the nucleus – spherical shaped void showing little fluorescent staining, in the  $x$ - $z$  plane (Fig. 2(A) and (B)). Given the outer diameter of a microtubule structure as  $\sim 25$  nm, and the size of primary and secondary labeling as  $\sim 17.5$  nm, the expected width (FWHM) of a cross-section profile of a microtubule can range from 70 to 92 nm depending on the achieved localization precision [45]. We quantified these resolved individual tubular structures by their intensity profiles in both lateral and axial directions (Fig. 2(D), and Appendix, Fig. 6(A) and (B)) and the average FWHMs in the lateral and axial directions are  $88 \pm 13$  nm and  $103 \pm 12$  nm (mean  $\pm$  std.,  $n = 30$ ) respectively.

We further imaged the nucleoporin protein Nup98, part of the nuclear pore complex (NPC), localized near the center channel of the NPC scaffold, immuno-labeled with Alexa Fluor 647 in fixed COS-7 cells. We observed that the axial plane SMLM system was capable of resolving individual labeled NPCs as isolated clusters in both lateral and axial directions whereas the conventional axial plane image resulted in diffraction-limited resolution where only the NPC-decorated membrane contour was discernible (Fig. 2(E) and (F)). From the quantitative measurements in both lateral and axial directions of thirty distinctly resolved NPCs (Appendix, Fig. 6(C) and (D)), we found the FWHMs in the lateral and axial directions as  $79 \pm 6$  nm and  $103 \pm 16$  nm (mean  $\pm$  std.,  $n = 30$ ) respectively. There was no significant difference in these measurements with respect to the imaging depth ( $\sim 8$   $\mu\text{m}$ ) (additional super-resolved images are shown in Appendix, Fig. 7).

### 3.3. Multiplexed super-resolution imaging with the axial plane SMLM and exchange-PAINT

DNA-PAINT and exchange-PAINT offer a robust and versatile labeling approach for SMLM, owing to the transient binding of “imager” strands to their complementary “docking” strands [30,31]. Comparing to conventional switchable SMLM probes, DNA-PAINT exhibits effectively nonexistent photobleaching with the near infinite supply of fresh “imager” strands from the buffer, and allows straightforward sequential imaging of multiple targets, namely exchange-PAINT [31]. However, these free-diffusing “imager” strands significantly contribute to fluorescence background during single-molecule imaging, limiting the majority of its applications to biological structures near the coverslip surface.

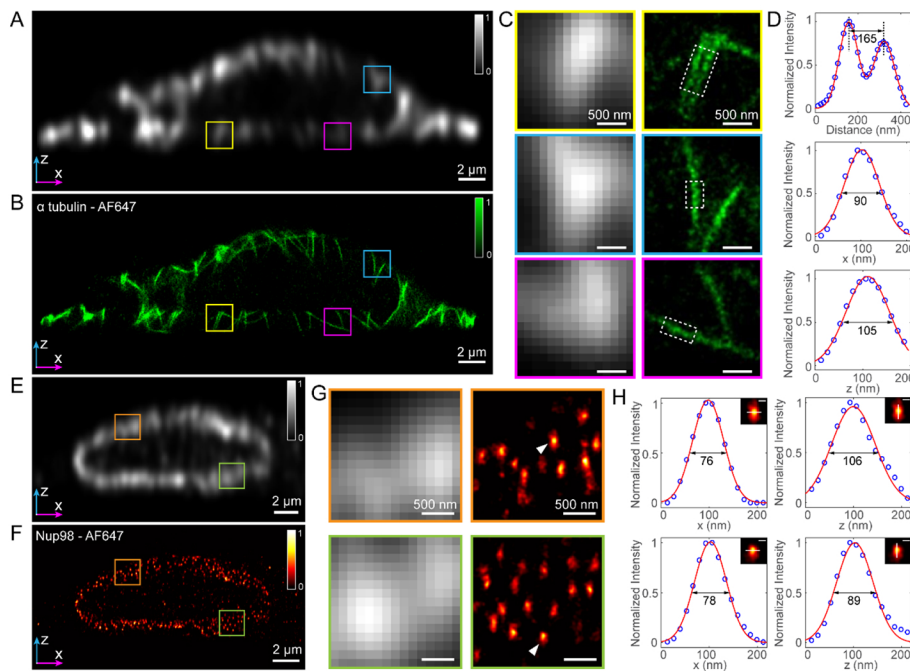


**Fig. 2.** Super-resolution reconstructions of microtubules and nuclear pore complexes by the axial plane SMLM in fixed COS-7 cells. (A) Diffraction-limited axial plane image of  $\alpha$ -tubulin immuno-labeled with Alexa Fluor 647 (AF647). (B) Axial plane super-resolution image of A. (C) Enlarged views of three microtubule segments marked in A and B with the yellow, blue, and magenta squares respectively. (D) Normalized intensity profiles of microtubules marked with the white dashed rectangles in C. (E) Diffraction-limited axial plane image of Nup98 immuno-labeled with AF647. (F) Axial plane super-resolution image of E. (G) Enlarged views of two regions marked in E and F with the orange and green squares respectively. (H) Normalized intensity profiles in the  $x$  and  $z$  directions of two nuclear pore complexes (NPCs) indicated by the white arrows in G. Scale bar: 2  $\mu\text{m}$  in A, B, E and F, 500 nm in C and G, 100 nm in H (insets).

The axial plane SMLM system allows super-resolution imaging of the axial plane throughout a whole cell and is compatible with DNA-PAINT and exchange-PAINT by virtue of its light-sheet illumination providing a highly confined excitation (light sheet FWHM  $1.19 \pm 0.04 \mu\text{m}$ , Appendix, Fig. 5(E)–(I)). The axial plane SMLM excites single molecules only at the axial optical section that is in focus on the detector but not the freely diffusing probes nor the out-of-focus docked probes and therefore minimizes the background.

To demonstrate DNA-PAINT imaging using the axial plane SMLM, we imaged immuno-labeled  $\alpha$ -tubulin with DNA-PAINT “docking” strands in fixed COS-7 cells, and with corresponding “imager” conjugated with Atto 655. From the acquired single-molecule blinking dataset, we observed a nearly 11-fold reduction of fluorescence background when comparing between light-sheet and epi illumination (Fig. 1(G) and (H)). While the significant fluorescence background, resulting from an ocean of free diffusing probes and out-of-focus docked probes, made single-molecule emissions difficult to observe by using epi illumination, it could be clearly visualized under light-sheet illumination in this system. In the reconstructed super-resolution image of microtubules network, we quantified the resolved individual tubulin profiles in both lateral and axial directions as 75 nm and 106 nm respectively (Appendix, Fig. 8).

The demonstrated compatibility of the axial plane SMLM with oligo-based probes allowed us to perform multiplexed super-resolution imaging using exchange-PAINT. Here we demonstrated multiplexed super-resolution imaging in the axial plane resolving both microtubules and mitochondria labeled with orthogonal DNA “docking” strands P1 and P4 in fixed COS-7 cells, respectively. We obtained multiplexed axial plane super-resolution images through whole cells in the axial cross-section, displaying super-resolved  $\alpha$ -tubulin and Tom20 through the same axial plane (Fig. 3 and Appendix, Fig. 9). We found that the axial distribution of these two cellular targets was organized spatially exclusively with individual microtubules extending alongside the Tom20-decorated mitochondria surface. In addition, by resolving multiple protein species with the same fluorescent dye, exchange-PAINT allowed multiplexed super-resolution imaging with a single laser source in excitation and without chromatic aberrations in emission.

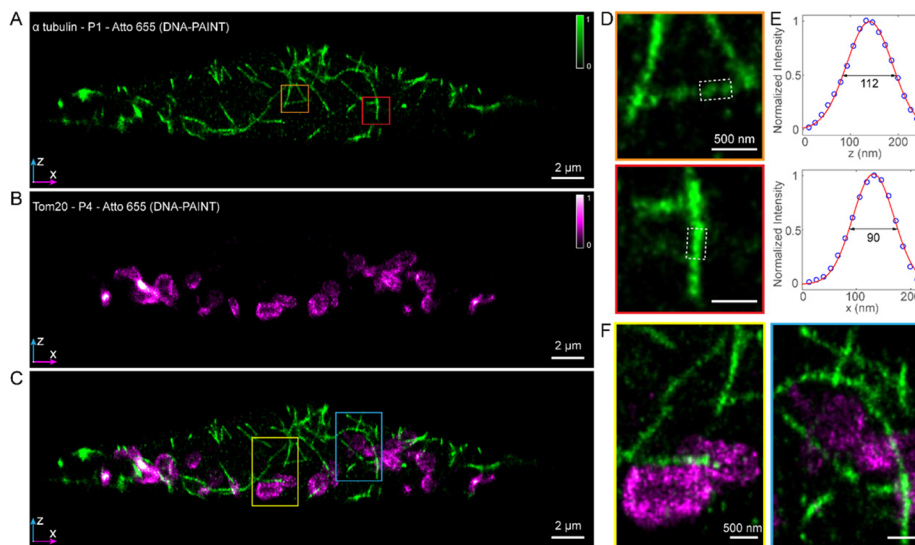


**Fig. 3.** Multiplexed axial plane super-resolution reconstructions of microtubules and mitochondria in COS-7 cells. (A) Axial plane super-resolution image of  $\alpha$ -tubulin labeled with anti-mouse P1 “docking” strands. (B) Axial plane super-resolution image of Tom20 labeled with anti-rabbit P4 “docking” strands (the same axial plane as A). (C) Two-channel combined image of  $\alpha$ -tubulin (green) and Tom20 (magenta) located in the same axial cross-section. (D) Enlarged views of two segments marked in A with the orange and red squares, respectively. (E) Normalized intensity profiles of microtubules marked with the white dashed rectangles in D. Two microtubules laying along the  $x$ -axis and  $z$ -axis showed averaged FWHMs in the  $z$  and  $x$  directions as 112 nm and 90 nm, respectively. (F) Enlarged views of two regions marked in C with the yellow and blue rectangles, respectively. The axial plane organization of microtubules and mitochondria were resolved. Scale bar: 2  $\mu$ m in A, B and C, 500 nm in D and F.

### 3.4. Resolving the nucleus of glioblastoma multiforme cells with the axial plane SMLM

Our presented SMLM system allows efficient super-resolution profiling of thick specimens in the axial plane. We demonstrated this unique compatibility of the axial plane SMLM with thick specimens by imaging immuno-labeled Nup98 in glioblastoma multiforme cells (GBM10 cells), whose cell height ranges from 10 to 30  $\mu$ m usually consisting a large nucleus (>10  $\mu$ m). Conventional imaging of a GBM10 cell throughout its extended height requires scanning in the axial direction with a step size usually 400 nm and subsequently ~50 optical sections

are required to reveal its axial profile. Using the axial plane SMLM, we were able to resolve Nup98-labeled nuclear envelope throughout the entire depth of the tumor cell without axial scanning. At various imaging depths, we found individual pores were distinctly resolved whereas their diffraction-limited counterparts blurred the individual NPCs into a continuous contour of the nucleus (Fig. 4). We observed consistent achieved resolution with different imaging depths as shown in Nup98 axial plane SMLM images with total depths of 14  $\mu\text{m}$  and 17  $\mu\text{m}$  (Fig. 4(A) and (D)). We measured localized Nup98 cluster profiles with a single reconstruction in the lateral direction at different imaging depths and found FWHMs of 66 nm and 69 nm at 1.8  $\mu\text{m}$  and 16.0  $\mu\text{m}$  respectively. The corresponding axial profiles displayed FWHMs of 93 nm and 95 nm respectively (Fig. 4(F)). Further studies of GBM10 immune response using multiplexed axial plane SMLM could allow axial profiling of multiple proteins (e.g. antigens) on these treatment-refractive cells to infer mechanisms driving immune response and to guide the development of more effective and safer immunotherapies.

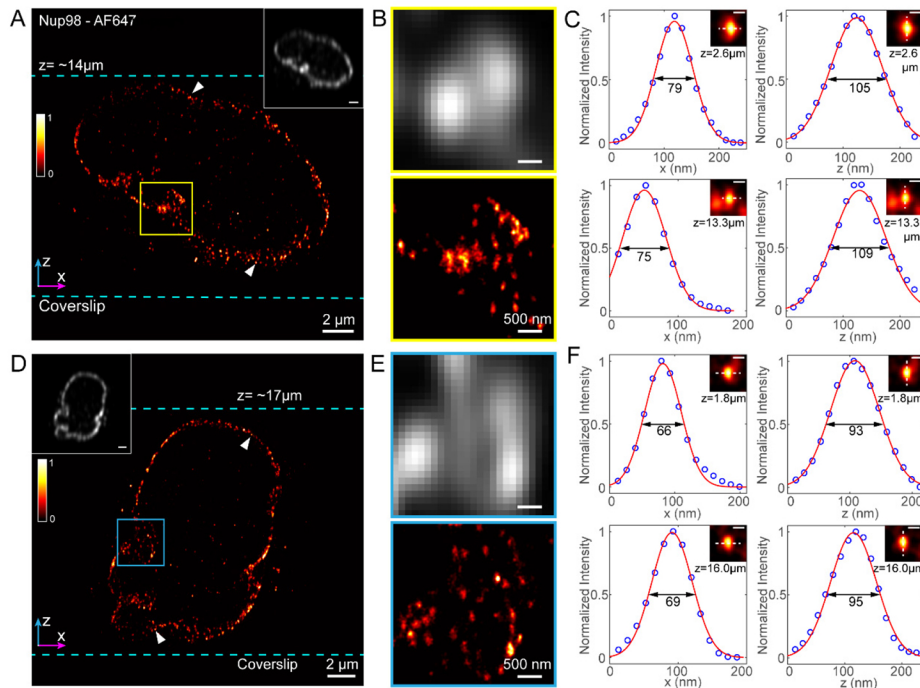


**Fig. 4.** Axial plane super-resolution reconstructions of immuno-labeled Nup98 in GBM10 cells. (A, D) Axial plane super-resolution images of Nup98 immuno-labeled with Alexa Fluor 647 (AF647). The insets show the corresponding diffraction-limited images. (B, E) Enlarged views of the regions marked in A with the yellow square and in D with the blue square, and the corresponding diffraction-limited images. (C, F) Normalized intensity profiles in the  $x$  and  $z$  directions of two NPCs located in different imaging depths ( $\sim 2.6 \mu\text{m}$  and  $13.3 \mu\text{m}$  in C,  $\sim 1.8 \mu\text{m}$  and  $16.0 \mu\text{m}$  in F) indicated by the white arrows in A and D, respectively. The FWHMs highlight the similar resolution in different imaging depths of the axial plane SMLM. Scale bar: 2  $\mu\text{m}$  in A, D and their insets, 500nm in B and E, 100 nm in C and F (insets).

#### 4. Conclusion

In this work, we developed an axial plane super-resolution system by integrating single-objective light-sheet illumination and axial plane optical imaging with single-molecule detection and localization. We demonstrated the proposed system by resolving the axial distribution of different subcellular targets such as microtubules, mitochondria and NPCs over the whole-cell depth. The presented axial plane SMLM is compatible with DNA-PAINT and exchange-PAINT due to its native light-sheet illumination and axial detection allowing multiplexed axial plane super-resolution imaging resolving multiple subcellular targets in a sequential manner. Due to the ability to achieve consistent resolution through an imaging depth, the system allows us to resolve individual nuclear pore complexes decorating the entire nuclear envelope in large glioblastoma patient-derived tumor cells. As a unique technique for efficient super-resolution profiling in the depth dimension, we hope the axial plane SMLM will be a useful tool to study intra- and extra-cellular structures and processes along the axial direction in both fixed and living specimens.

#### Appendix: Figs. 5 to 9

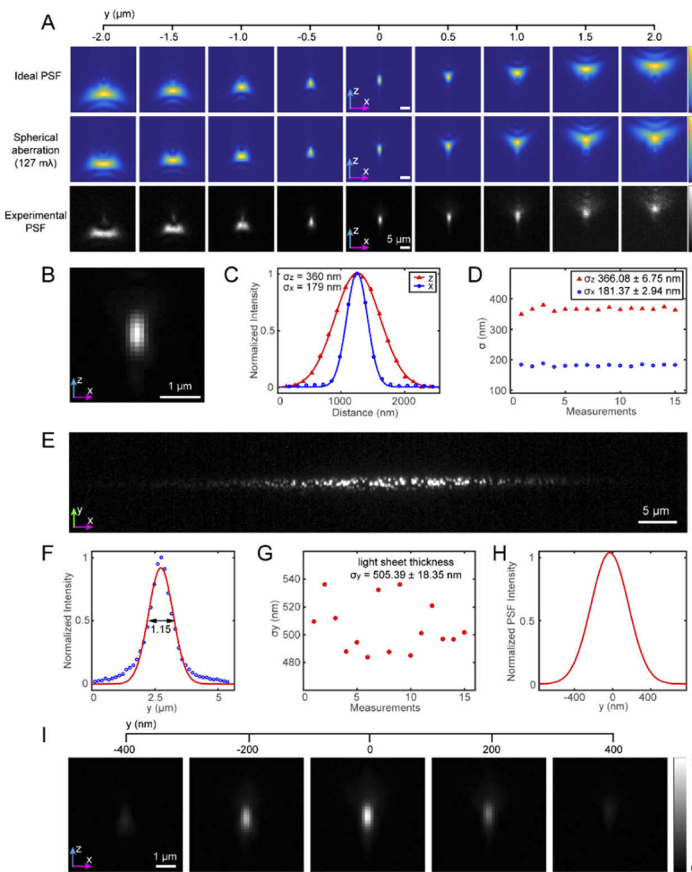


**Fig. 5.** Simulated and experimental axial plane PSFs of the axial plane SMLM system. (A) Simulated ideal axial plane PSFs, scanning along the  $y$ -axis (first row). The simulated axial plane PSFs with a small amount of primary spherical aberration  $\sim 127 \text{ m}\lambda$  (second row). The experimental axial plane PSFs acquired with a 100 nm-diameter crimson bead excited by epi illumination, scanning along the  $y$ -axis by sample stage (third row). (B) Experimental in-focus PSF. It is the effective PSF used for single-molecule localization. (C) Intensity profiles along the long (i.e.  $z$ ) and short (i.e.  $x$ ) axes of the experimental elliptical PSF in B, respectively. (D) Distributions of  $\sigma_x$  and  $\sigma_z$  which is  $181.37 \pm 2.94 \text{ nm}$  for the short axis and  $366.08 \pm 6.75 \text{ nm}$  for the long axis (mean  $\pm$  std.,  $n = 15$ ), measured from the experimental in-focus PSFs. (E) Image of dense fluorescence beads excited by a light sheet. (F) Intensity profile of the light sheet of E in the  $y$  direction, with the FWHM of  $1.15 \mu\text{m}$ . (G) Distribution of  $\sigma_y$  of the light sheet thickness measured 15 different light sheets, with the  $\sigma_y$  of  $505.39 \pm 18.35 \text{ nm}$  (mean  $\pm$  std.,  $n = 15$ ), corresponding to a FWHM of  $1.19 \pm 0.04 \mu\text{m}$ . (H) Distribution of the detected PSF intensity (with the localization sub-region as  $1.5 \times 1.5 \mu\text{m}^2$ ) along the  $y$ -axis. The PSF intensity becomes significantly dimmer outside the range of  $\pm 300 \text{ nm}$ . (I) Experimental axial plane PSFs acquired with a 100 nm-diameter crimson bead excited by the light sheet, scanning along the  $y$ -axis. Scale bar: 5 μm in A and E, 1 μm in B and I.

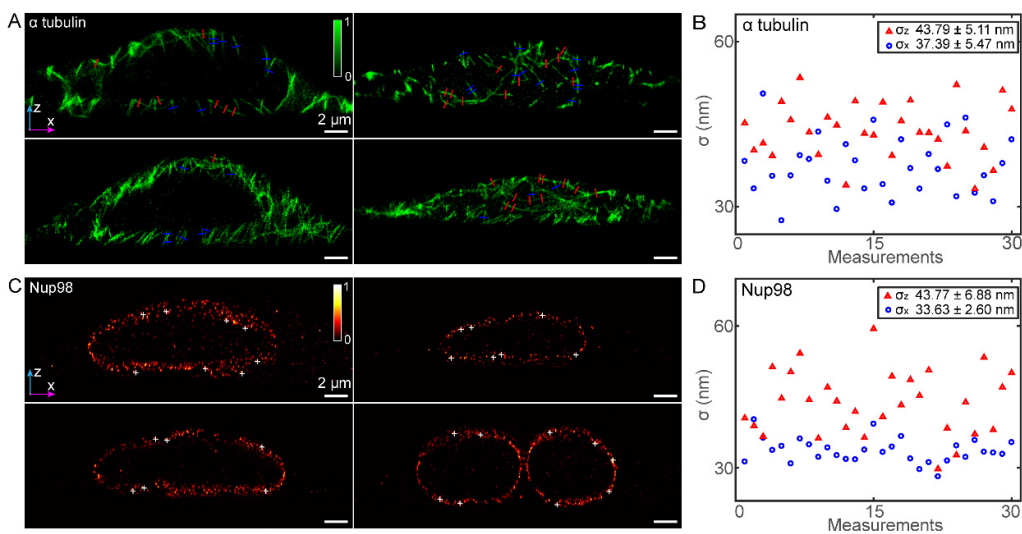


**Fig. 6.** Localization precision quantifications of the axial plane SMLM. (A) Axial plane super-resolution images of  $\alpha$ -tubulin in different COS-7 cells. (B) Distributions of  $\sigma_x$  ( $37.39 \pm 5.47$  nm, blue circles) and  $\sigma_z$  ( $43.79 \pm 5.11$  nm, red triangles), measured from 30 microtubules laying approximately along the  $z$ -axis (marked with the blue lines in A) and 30 microtubules laying approximately along the  $x$ -axis (marked with the red lines in A), respectively. (C) Axial plane super-resolution images of Nup98 in different COS-7 cells. (D) Distributions of  $\sigma_x$  ( $33.63 \pm 2.60$  nm, blue circles) and  $\sigma_z$  ( $43.77 \pm 6.88$  nm, red triangles), measured from 30 NPCs (marked with the white crosses in C). Scale bar: 2  $\mu$ m in A and C.

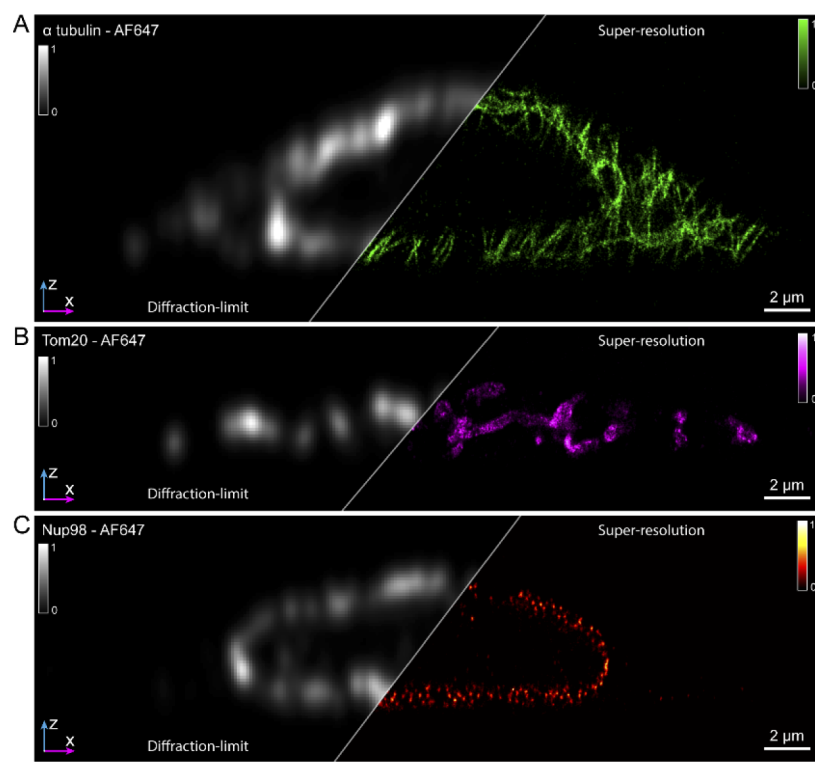


**Fig. 7.** Axial plane super-resolution reconstructions of different targets in fixed COS-7 cells. (A, B, C) Axial plane diffraction-limited (left) and the corresponding super-resolution (right) images of  $\alpha$ -tubulin (A), Tom20 (B), and Nup98 (C), all immuno-labeled with Alexa Fluor 647 (AF647). Scale bar: 2  $\mu$ m.

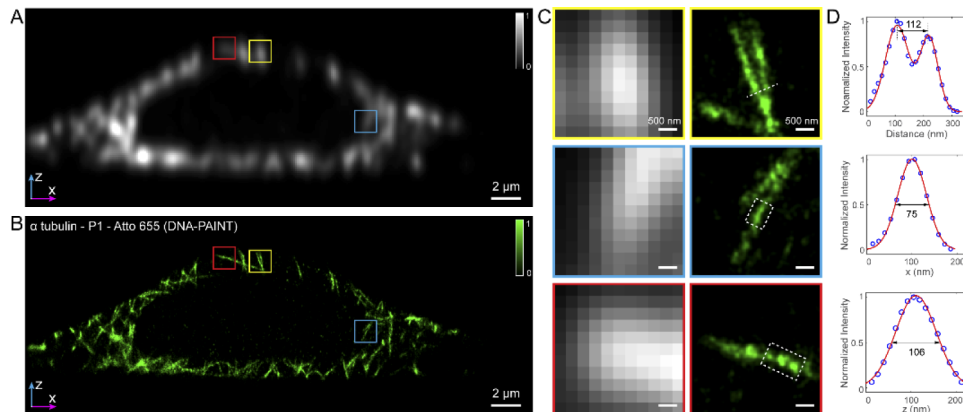


**Fig. 8.** Single-channel axial plane super-resolution reconstruction by combining the axial plane SMLM with DNA-PAINT. (A) Diffraction-limited axial plane image of  $\alpha$ -tubulin labeled with anti-mouse P1 “docking” strands. (B) Axial plane super-resolution image of A. (C) Enlarged views of three microtubule segments marked in A and B with the yellow, blue, and red squares respectively. (D) Normalized intensity profiles of microtubules marked with the white dashed line and rectangles in C. Comparable resolution was achieved as the conventional SMLM probe Alexa Fluor 647 (Fig. 2). Scale bar: 2  $\mu$ m in A and B, 500 nm in C.

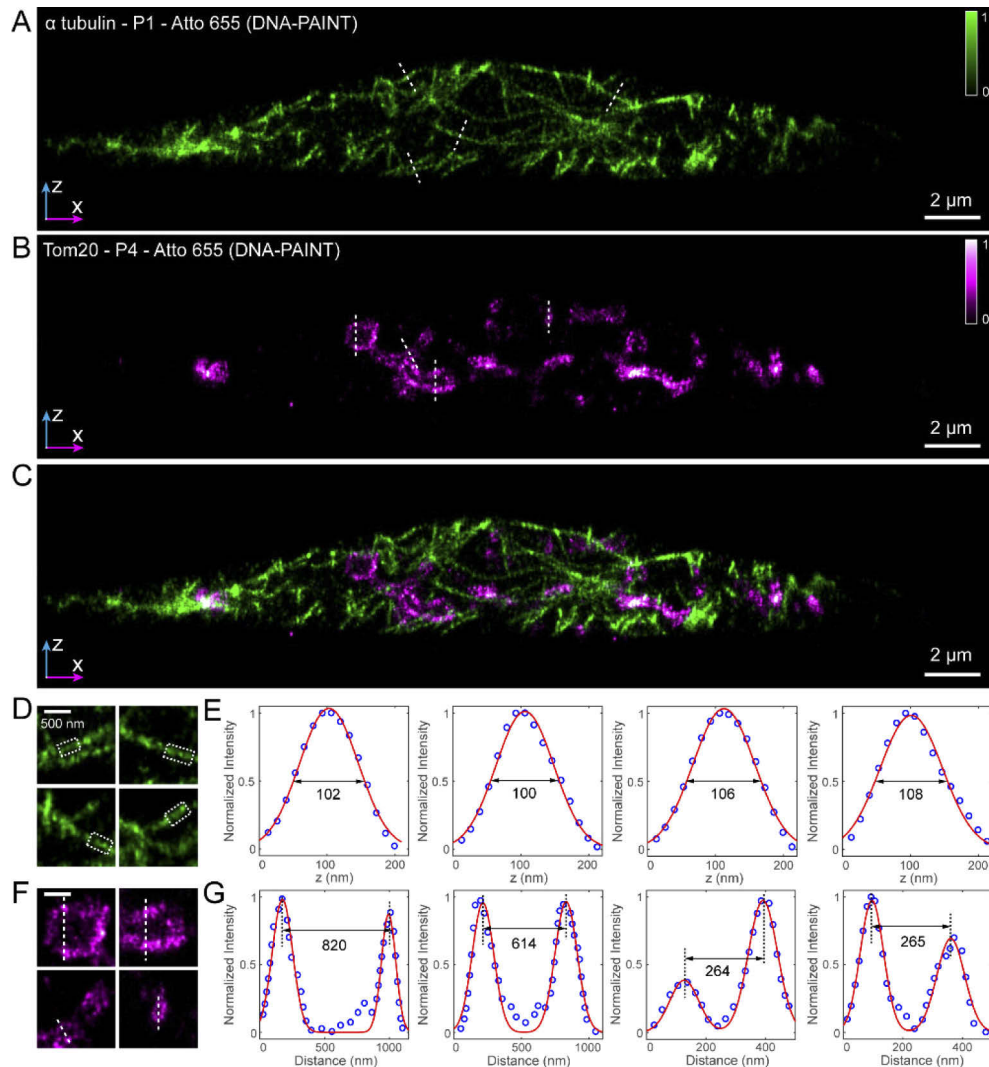


**Fig. 9.** Multiplexed axial plane super-resolution reconstructions of microtubules and mitochondria in fixed COS-7 cells. (A) Axial plane super-resolution image of  $\alpha$ -tubulin labeled with anti-mouse P1 “docking” strands. (B) Axial plane super-resolution image of Tom20 labeled with anti-rabbit P4 “docking” strands (the same axial plane as A). (C) Two-channel combined image of  $\alpha$ -tubulin (green) and Tom20 (magenta) located in the same axial cross-section. (D) Enlarged views of microtubule segments marked in A with the white dashed lines. (E) Normalized intensity profiles of microtubules laying approximately along the  $x$ -axis marked with the white dashed rectangles in D, with FWHMs of 102 nm, 100 nm, 106 nm and 108 nm in the  $z$  direction, respectively. (F) Enlarged views of mitochondria segments marked in B with the white dashed lines. (G) Normalized intensity profiles of mitochondria marked with the white dashed lines in F, with different membrane distances of 820 nm, 614 nm, 264 nm and 265 nm, respectively. Scale bar: 2  $\mu$ m in A, B and C, 500 nm in D and F.

## Funding

National Institute of General Medical Sciences (R35GM119785); Defense Advanced Research Projects Agency (D16AP00093); National Institutes of Health (1R01EB018659, 1R01GM124401).

## Acknowledgements

We would like to thank Karthigeyan Dhanasekaran and Patrick Lusk (Yale University) for sharing the labeling protocol of Nup98 and interpretation of the resolved Nup98 structures, and David A. Miller for providing labeling protocols of mitochondria and microtubules. We thank Sheng Liu and Donghan Ma for helpful discussions on instrument alignment and sample labeling.

## Disclosures

P.Y. holds patent related to DNA-PAINT and is co-founder of Ultivue Inc and NuProbe Global.

## References

1. S. W. Hell, "Far-field optical nanoscopy," *Science* **316**(5828), 1153–1158 (2007).
2. S. W. Hell and J. Wichmann, "Breaking the diffraction resolution limit by stimulated emission: stimulated-emission-depletion fluorescence microscopy," *Opt. Lett.* **19**(11), 780–782 (1994).
3. T. A. Klar and S. W. Hell, "Subdiffraction resolution in far-field fluorescence microscopy," *Opt. Lett.* **24**(14), 954–956 (1999).
4. M. Hofmann, C. Eggeling, S. Jakobs, and S. W. Hell, "Breaking the diffraction barrier in fluorescence microscopy at low light intensities by using reversibly photoswitchable proteins," *Proc. Natl. Acad. Sci. U. S. A.* **102**(49), 17565–17569 (2005).
5. M. G. Gustafsson, "Surpassing the lateral resolution limit by a factor of two using structured illumination microscopy," *J. Microsc.* **198**(2), 82–87 (2000).
6. M. G. Gustafsson, "Nonlinear structured-illumination microscopy: wide-field fluorescence imaging with theoretically unlimited resolution," *Proc. Natl. Acad. Sci. U. S. A.* **102**(37), 13081–13086 (2005).
7. Y. Wu and H. Shroff, "Faster, sharper, and deeper: structured illumination microscopy for biological imaging," *Nat. Methods* **15**(12), 1011–1019 (2018).
8. E. Betzig, G. H. Patterson, R. Sougrat, O. W. Lindwasser, S. Olenych, J. S. Bonifacino, M. W. Davidson, J. Lippincott-Schwartz, and H. F. Hess, "Imaging intracellular fluorescent proteins at nanometer resolution," *Science* **313**(5793), 1642–1645 (2006).
9. S. T. Hess, T. P. Girirajan, and M. D. Mason, "Ultra-high resolution imaging by fluorescence photoactivation localization microscopy," *Biophys. J.* **91**(11), 4258–4272 (2006).
10. M. J. Rust, M. Bates, and X. Zhuang, "Sub-diffraction-limit imaging by stochastic optical reconstruction microscopy (STORM)," *Nat. Methods* **3**(10), 793–796 (2006).
11. B. Huang, W. Wang, M. Bates, and X. Zhuang, "Three-dimensional super-resolution imaging by stochastic optical reconstruction microscopy," *Science* **319**(5864), 810–813 (2008).
12. C. S. Smith, N. Joseph, B. Rieger, and K. A. Lidke, "Fast, single-molecule localization that achieves theoretically minimum uncertainty," *Nat. Methods* **7**(5), 373–375 (2010).
13. F. Huang, T. M. Hartwich, F. E. Rivera-Molina, Y. Lin, W. C. Duim, J. J. Long, P. D. Uchil, J. R. Myers, M. A. Baird, W. Mothes, and M. W. Davidson, "Video-rate nanoscopy using sCMOS camera-specific single-molecule localization algorithms," *Nat. Methods* **10**(7), 653–658 (2013).
14. F. Huang, G. Sirinakis, E. S. Allgeyer, L. K. Schroeder, W. C. Duim, E. B. Kromann, T. Phan, F. E. Rivera-Molina, J. R. Myers, I. Irnov, and M. Lessard, "Ultra-high resolution 3D imaging of whole cells," *Cell* **166**(4), 1028–1040 (2016).
15. K. I. Mortensen, L. S. Churchman, J. A. Spudich, and H. Flyvbjerg, "Optimized localization analysis for single-molecule tracking and super-resolution microscopy," *Nat. Methods* **7**(5), 377–381 (2010).
16. S. Manley, J. M. Gillette, G. H. Patterson, H. Shroff, H. F. Hess, E. Betzig, and J. Lippincott-Schwartz, "High-density mapping of single-molecule trajectories with photoactivated localization microscopy," *Nat. Methods* **5**(2), 155–157 (2008).
17. D. Aquino, A. Schönlé, C. Geisler, C. v Middendorff, C. A. Wurm, Y. Okamura, T. Lang, S. W. Hell, and A. Egner, "Two-color nanoscopy of three-dimensional volumes by 4Pi detection of stochastically switched fluorophores," *Nat. Methods* **8**(4), 353–359 (2011).
18. B. Huang, S. A. Jones, B. Brandenburg, and X. Zhuang, "Whole-cell 3D STORM reveals interactions between cellular structures with nanometer-scale resolution," *Nat. Methods* **5**(12), 1047–1052 (2008).
19. M. J. Mlodzianoski, P. J. Cheng-Hathaway, S. M. Bemiller, T. J. McCray, S. Liu, D. A. Miller, B. T. Lamb, G. E. Landreth, and F. Huang, "Active PSF shaping and adaptive optics enable volumetric localization microscopy through brain sections," *Nat. Methods* **15**(8), 583–586 (2018).

20. P. J. Keller and E. H. Stelzer, "Quantitative *in vivo* imaging of entire embryos with digital scanned laser light sheet fluorescence microscopy," *Curr. Opin. Neurobiol.* **18**(6), 624–632 (2008).
21. A. Maizel, D. von Wangenheim, F. Federici, J. Haseloff, and E. H. Stelzer, "High-resolution live imaging of plant growth in near physiological bright conditions using light sheet fluorescence microscopy," *Plant J.* **68**(2), 377–385 (2011).
22. B. C. Chen, W. R. Legant, K. Wang, L. Shao, D. E. Milkie, M. W. Davidson, C. Janetopoulos, X. S. Wu, J. A. Hammer, Z. Liu, and B. P. English, "Lattice light-sheet microscopy: imaging molecules to embryos at high spatiotemporal resolution," *Science* **346**(6208), 1257998 (2014).
23. J. C. M. Gebhardt, D. M. Suter, R. Roy, Z. W. Zhao, A. R. Chapman, S. Basu, T. Maniatis, and X. S. Xie, "Single-molecule imaging of transcription factor binding to DNA in live mammalian cells," *Nat. Methods* **10**(5), 421–426 (2013).
24. Z. W. Zhao, R. Roy, J. C. M. Gebhardt, D. M. Suter, A. R. Chapman, and X. S. Xie, "Spatial organization of RNA polymerase II inside a mammalian cell nucleus revealed by reflected light-sheet superresolution microscopy," *Proc. Natl. Acad. Sci. U. S. A.* **111**(2), 681–686 (2014).
25. R. Galland, G. Gencic, A. Aravind, V. Viasnoff, V. Studer, and J. B. Sibarita, "3D high-and super-resolution imaging using single-objective SPIM," *Nat. Methods* **12**(7), 641–644 (2015).
26. M. B. Meddens, S. Liu, P. S. Finnegan, T. L. Edwards, C. D. James, and K. A. Lidke, "Single objective light-sheet microscopy for high-speed whole-cell 3D super-resolution," *Biomed. Opt. Express* **7**(6), 2219–2236 (2016).
27. A. K. Gustavsson, P. N. Petrov, M. Y. Lee, Y. Shechtman, and W. E. Moerner, "3D single-molecule super-resolution microscopy with a tilted light sheet," *Nat. Commun.* **9**(1), 123 (2018).
28. T. Li, S. Ota, J. Kim, Z. J. Wong, Y. Wang, X. Yin, and X. Zhang, "Axial plane optical microscopy," *Sci. Rep.* **4**(1), 7253 (2015).
29. J. Kim, M. Wojcik, Y. Wang, S. Moon, E. A. Zin, N. Marnani, Z. L. Newman, J. G. Flannery, K. Xu, and X. Zhang, "Oblique-plane single-molecule localization microscopy for tissues and small intact animals," *Nat. Methods* **16**(9), 853–857 (2019).
30. R. Jungmann, C. Steinhauer, M. Scheible, A. Kuzyk, P. Tinnefeld, and F. C. Simmel, "Single-molecule kinetics and super-resolution microscopy by fluorescence imaging of transient binding on DNA origami," *Nano Lett.* **10**(11), 4756–4761 (2010).
31. R. Jungmann, M. S. Avendaño, J. B. Woehrstein, M. Dai, W. M. Shih, and P. Yin, "Multiplexed 3D cellular super-resolution imaging with DNA-PAINT and Exchange-PAINT," *Nat. Methods* **11**(3), 313–318 (2014).
32. J. Schnitzbauer, M. T. Strauss, T. Schlichthaerle, F. Schueder, and R. Jungmann, "Super-resolution microscopy with DNA-PAINT," *Nat. Protoc.* **12**(6), 1198–1228 (2017).
33. F. Schueder, J. Lara-Gutiérrez, B. J. Beliveau, S. K. Saka, H. M. Sasaki, J. B. Woehrstein, M. T. Strauss, H. Grabmayr, P. Yin, and R. Jungmann, "Multiplexed 3D super-resolution imaging of whole cells using spinning disk confocal microscopy and DNA-PAINT," *Nat. Commun.* **8**(1), 2090 (2017).
34. S. S. Agasti, Y. Wang, F. Schueder, A. Sukumar, R. Jungmann, and P. Yin, "DNA-barcoded labeling probes for highly multiplexed Exchange-PAINT imaging," *Chem. Sci.* **8**(4), 3080–3091 (2017).
35. Y. Wang, J. B. Woehrstein, N. Donoghue, M. Dai, M. S. Avendaño, R. C. Schackmann, J. J. Zoeller, S. S. H. Wang, P. W. Tillberg, D. Park, and S. W. Lapan, "Rapid sequential *in situ* multiplexing with DNA exchange imaging in neuronal cells and tissues," *Nano Lett.* **17**(10), 6131–6139 (2017).
36. R. E. Thompson, D. R. Larson, and W. W. Webb, "Precise nanometer localization analysis for individual fluorescent probes," *Biophys. J.* **82**(5), 2775–2783 (2002).
37. X. Li, P. Mooney, S. Zheng, C. R. Booth, M. B. Braunfeld, S. Gubbens, D. A. Agard, and Y. Cheng, "Electron counting and beam-induced motion correction enable near-atomic-resolution single particle cryo-EM," *Nat. Methods* **10**(6), 584–590 (2013).
38. Y. Wang, J. Schnitzbauer, Z. Hu, X. Li, Y. Cheng, Z. L. Huang, and B. Huang, "Localization events-based sample drift correction for localization microscopy with redundant cross-correlation algorithm," *Opt. Express* **22**(13), 15982–15991 (2014).
39. R. McGorty, D. Kamiyama, and B. Huang, "Active microscope stabilization in three dimensions using image correlation," *Opt. Nano.* **2**(1), 3 (2013).
40. S. Coelho, M. S. Graus, J. M. Halstead, P. R. Nicovich, K. Feher, H. Gandhi, and K. Gaus, "Single molecule localization microscopy with autonomous feedback loops for ultrahigh precision," *bioRxiv* 487728 (2018).
41. J. Kim, T. Li, Y. Wang, and X. Zhang, "Vectorial point spread function and optical transfer function in oblique plane imaging," *Opt. Express* **22**(9), 11140–11151 (2014).
42. S. Liu, E. B. Kromann, W. D. Krueger, J. Bewersdorf, and K. A. Lidke, "Three dimensional single molecule localization using a phase retrieved pupil function," *Opt. Express* **21**(24), 29462–29487 (2013).
43. P. Zhang, S. Liu, A. Chaurasia, D. Ma, M. J. Mlodzianoski, E. Culurciello, and F. Huang, "Analyzing complex single-molecule emission patterns with deep learning," *Nat. Methods* **15**(11), 913–916 (2018).
44. S. F. Gibson and F. Lanni, "Experimental test of an analytical model of aberration in an oil-immersion objective lens used in three-dimensional light microscopy," *J. Opt. Soc. Am. A* **8**(10), 1601–1613 (1991).
45. A. Aristov, B. Lelandais, E. Rensen, and C. Zimmer, "ZOLA-3D allows flexible 3D localization microscopy over an adjustable axial range," *Nat. Commun.* **9**(1), 2409 (2018).